IEEE Sensors Council

# A Shin-mounted Inertial Navigation System for Pedestrian Walking and Running Gait

Jian Kuang, Dazhou Xia, Yan Wang, Xianmei Meng and Xiaoji Niu

*Abstract*— **Accurately and reliably estimating the position of pedestrians with complex gaits is a primary challenge for current positioning solutions using wearable inertial sensors. This paper proposes a novel zero-velocity detection method tailored for walking and running using a shin-mounted IMU, resulting in a shin-mounted INS (Shin-INS) suitable for pedestrians with walking and running gaits. The proposed method divides pedestrian motion into stationary, walking and running stages, and designs zero-velocity detection signal features and methods according to the gait. On this basis, the zero-velocity update technique (ZUPT) and zero-position increment update method are used to achieve reliable pedestrian position estimation. We conducted over 30 tests, encompassing various running speeds, trajectory shapes, and transitions between walking and running gaits. The results demonstrate that the proposed method accurately estimates pedestrian motion trajectories, reducing positioning error by more than 30% under conditions of walking and running gait transitions compared to the Foot-INS based on adaptive threshold.**



*Index Terms*— **Pedestrian dead reckoning (PDR), foot-mounted inertial navigation system (Foot-INS), shin-mounted inertial navigation system (Shin-INS), pedestrian navigation.**
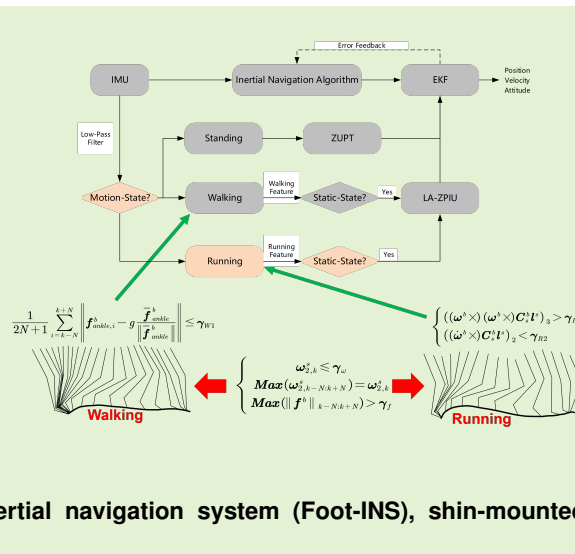
## I. INTRODUCTION

**H**IGH-precision and high-reliability pedestrian positioning systems (PNS) are fundamental to location-based services (LBS) [1]. While global navigation satellite systems (GNSS) effectively provide location services in open outdoor environments, meeting the general needs of mass users, their performance significantly deteriorates in environments with signal obstructions such as dense forests, urban canyons, tunnels, and indoor spaces. To address these limitations, various alternative positioning methods have been proposed [2], such as Wi-Fi [3], BLE [4], ultra-wideband (UWB) [5], magnetic field matching (MFM) [6], [7], and inertial navigation [8]. Among these, inertial navigation systems (INS) are particularly prominent as they enable pedestrian autonomous positioning without relying on any prior environmental information.

J. Kuang, Y. Wang and X. Niu are with the GNSS Research Center, Wuhan University, Wuhan, Hubei, CO 430072 PR China. X. Niu is also with the Hubei Luojia Laboratory. (E-mails: kuang@whu.edu.cn; wystephen@whu.edu.cn; xjniu@whu.edu.cn).
D. Xia is with the School of Geodesy and Geomatics, Wuhan University, Wuhan, Hubei, CO 430072 PRChina.(E-mails: dzhxia@whu.edu.cn).
X. Meng is with the School of Nursing, Wuhan University, Wuhan, Hubei, CO 430072 PRChina. (Email: hopemengmei@163.com).

INS based on Micro-Electro-Mechanical System Inertial Measurement Unit (MEMS-IMU) offer advantages of low cost and convenience but face the inevitable challenge of rapid position error accumulation. Pedestrian Dead Reckoning (PDR) based on MEMS-IMUs is an inertial navigation method specifically designed for pedestrian users, integrating pedestrian gait information with INS to achieve higher accuracy in position estimation. PDR can be categorized into Step-Model-Based PDR (S-PDR) and Foot-Mounted Inertial Navigation Systems (Foot-INS). S-PDR is a widely used method that allows flexible installation of IMUs (applicable to almost any part of the human body). It utilizes IMU measurements to detect steps and estimate the user's step length, combining sensor-estimated walking direction to track the user's position [8], [9]. However, S-PDR faces significant challenges in positioning performance degradation because the empirical step length model is not universally applicable to all users. Additionally, the walking direction estimation method based on the Attitude and Heading Reference System (AHRS) does not accurately capture the difference between the sensor's direction and the actual walking direction.

Foot-INS leverage the high relative accuracy of inertial navigation over short periods (e.g., 1 second) and utilize the periodic contact between the feet and the ground to establish virtual zero-velocity observations. By correcting accumulated velocity errors in the inertial navigation system, Foot-INS achieve continuous and reliable position estimation. The effec-

tiveness of the Foot-INS algorithm heavily relies on the accuracy of zero-velocity detection. Skog proposed a generalized likelihood ratio test (GLRT) detector, which operates under the assumption of zero angular rate and gravitational acceleration during the static phase [10]. This detector has gained widespread acceptance and is currently the most popular zero-velocity detector, particularly for standard walking gait, where it demonstrates impressive zero-velocity detection accuracy. However, the fixed threshold-based GLRT shows significant limitations when adapting to complex gaits.

Many advancements have been proposed to enhance the positioning performance of Foot-INS in complex gaits. Building on the GLRT detector, Wang developed an adaptive zero-velocity detection method utilizing clustering techniques, demonstrating superior detection stability in normal walking gait compared to the traditional GLRT approach [11]. Wahlström employed Bayesian theory and loss factors to establish an optimal threshold for zero-velocity detection under varying walking paces [12]. WagStaff trained a long short-term memory (LSTM) neural network capable of identifying and outputting zero-velocity interval across different walking gait [13]. Kone proposed a machine learning-based unified model designed to detect zero-velocity interval within each gait cycle, effectively adapting to diverse gait including walking, running, and ascending or descending stairs [14]. Cho divided the foot state into static and dynamic phases, combining characteristics of ground contact and lift-off along with step detection methods to achieve accurate zero-velocity interval detection under complex gaits [15]. However, these adaptive threshold methods face challenges in maintaining usability when dealing with complex gaits. Rule-based methods often constrain the user's movement pattern, and regular features may disappear under complex gaits. Although machine learning-based methods show high accuracy in zero-velocity detection, their performance relies on the scale and diversity of the training dataset. Consequently, they may suffer significant performance degradation in scenarios involving unknown users.

Under complex gaits, the foot does not behave as a rigid body, leading to ground contact at varying positions. Consequently, there might not be a strict zero-velocity interval at the IMU installation position, fundamentally causing a decline in zero-velocity detection accuracy and positioning performance of Foot-INS. To address this issue, we proposed the shin-mounted INS (Shin-INS) [9], which achieves positioning performance comparable to or even better than Foot-INS under normal walking gait. Additionally, Shin-INS offers the advantage of not requiring special shoes and being more user-friendly. However, the existing Shin-INS is not suitable for gait switching scenarios between walking and running. To address this limitation, this paper proposes a robust zero-velocity detection method for Shin-INS, enabling reliable pedestrian position estimation under complex gaits.

The remainder of this paper is organized as follows: The movement analysis of walking and running is provided in Section II, and a robust zero-velocity detection algorithm is proposed in Section III. In Section IV, a shin-mounted inertial navigation system is proposed. Section V presents the experimental results, and finally, Section VI concludes this

paper and proposes a direction for future work.

## II. MOVEMENT ANALYSIS OF WALKING AND RUNNING

Walking and running are the two most common pedestrian gaits. Although they share some basic dynamics and kinematics, there are significant differences between them. The transition from walking to running involves sudden changes in kinematics and dynamics [16]. For instance, the foot's contact time with the ground decreases by about 35% when transitioning from walking to running, while the peak ground reaction force increases by about 50%. Additionally, as the pedestrian's speed increases, the step length increases, while the gait cycle length and foot support duration decrease.

The transition between walking and running occurs because the human body seeks the most energy-efficient mode of movement at different speeds. This transition is fundamentally driven by inherent differences in movement structure and energy consumption. Fig. 1 illustrates a model of the lower limb's contact with the ground during walking and running. During walking, the lower limb functions like an inverted pendulum, with the body passing over the supporting leg in an arc. In the first half of the stance phase, kinetic energy is converted into gravitational potential energy, which is then released in the second half of the stance phase as the body leans forward and downward. In contrast, during running, the lower limb operates more like a pogo stick. When the foot contacts the ground during running, kinetic energy and gravitational potential energy are temporarily stored in the muscles, tendons, and ligaments as elastic strain energy. This stored energy is then released in the second half of the stance phase, providing the necessary propulsion [16].

We previously proposed a method for detecting zero-velocity intervals based on zero acceleration when the ankle touches the ground. This zero acceleration is obtained by projecting the shin-mounted IMU measurement to the ankle joint through lever compensation. Experiments have shown that this zero-velocity detection method is applicable to various gaits, including normal walking, lateral walking, and oblique walking. However, as depicted in Fig. 1, the acceleration projected from the shin-mounted IMU to the ankle joint during the running contact phase is not zero. Therefore, the zero-velocity detection method designed for walking gait is not applicable to running gait. To address this, it is essential to effectively distinguish between walking and running gaits and manage the differences in kinematics, dynamics, and motion structure between these gaits. This will enable the development of a reliable zero-velocity detection method suitable for complex gaits.

## III. ROBUST ZERO-VELOCITY DETECTION ALGORITHM

Due to the intrinsic differences between walking and running gaits, this section first distinguishes the pedestrian motion states into walking and running, and then uses the signal features in different gaits to detect zero-velocity interval.
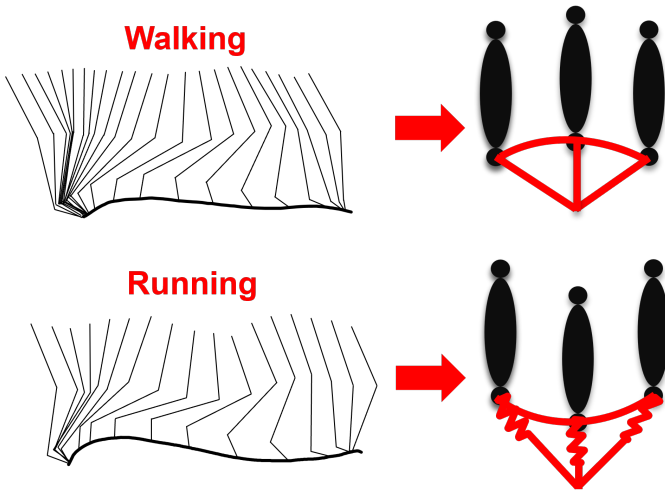
Fig. 1: Differences in gait between walking and running [16].
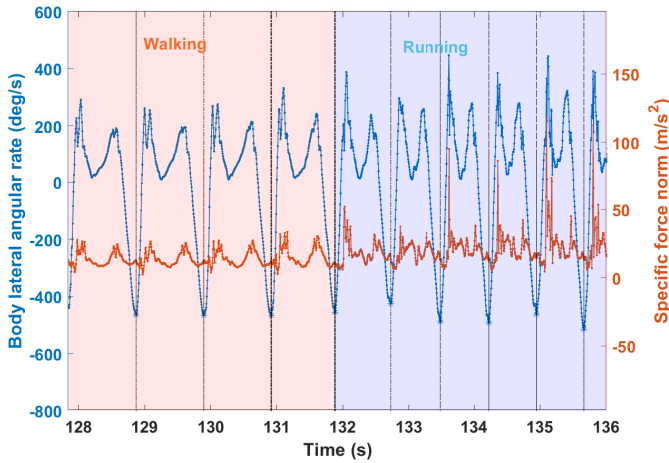


Fig. 2: Gait classification based on specific force modulus and body lateral angular rate.

## A. Gait Classification

Compared to step speed or the Froude number (a dimensionless parameter that considers leg length), step frequency has proven to be a more effective discriminant of gait. Chase uses a heuristic cadence threshold of 135-140 steps per minute, achieving a classification accuracy of 92.9% on a dataset containing young and middle-aged individuals [17]. Based on these findings, we selected step frequency as the feature to distinguish between running and walking states. Fig. 2 shows the specific force norm and body lateral angular rate from shin-mounted IMU measurements. There are distinct lateral angular rate troughs corresponding to each step. By detecting these troughs and calculating the time intervals between them, step frequency can be easily determined. This is because each gait cycle includes swing and support phases, with the troughs in the shin lateral angular rate occurring during the swing phase. Therefore, a window is established to detect and analyze the trough distance in real time, allowing for accurate determination of step frequency.

The criteria for gait classificationare as follows:

$$\begin{cases} \boldsymbol{\omega}_{2,k}^s \leqslant \boldsymbol{\gamma}_\omega \\ Max\left(\boldsymbol{\omega}_{2,k-N:k+N}^s\right) = \boldsymbol{\omega}_{2,k}^s \\ Max\left(\parallel \boldsymbol{f}^b \parallel_{k-N:k+N}\right) > \boldsymbol{\gamma}_f \end{cases} \quad (1)$$

where $\boldsymbol{\omega}_2^s$ is the second component of $\boldsymbol{\omega}^s$ (i.e., the lateral angular rate), $\parallel \boldsymbol{f}^b \parallel$ is the specific force modulus, $\gamma_f$ and $\boldsymbol{\gamma}_\omega$ are the given empirical threshold is the empirical threshold, $k$ is the $k$-th epoch, step detection window length is $2N+1$. The relationship between the sensor frame ($b$-frame) and the shin frame ($s$-frame) is as follows

$$\boldsymbol{\omega}^s = \boldsymbol{C}_b^s \boldsymbol{\omega}^b \quad (2)$$

where $\boldsymbol{C}_b^s$ includes the unknown parameters of roll, pitch and heading. The roll and pitch angles are determined using accelerometer data during the initialization phase, under the assumption that pedestrians are walking on a horizontal plane. The heading angle is estimated using principal component analysis (PCA). The basic principle is to project the accelerometer signals onto the horizontal plane, utilizing the observation that the pedestrian's direction of movement corresponds to the direction with the largest acceleration variance [18]. PCA is applied to the linear acceleration readings during the user's horizontal movement to obtain the final heading angle [19].

## B. Zero-Velocity Detection during Walking

During the interval in which a pedestrian's foot touches the ground in normal walking gait, the shin-mounted IMU rotates around the fixed point of the ankle. The lever arm compensation method, commonly used in integrated navigation, can effectively eliminate this rotational effect. This conclusion has been thoroughly verified in our previous work. The zero-velocity detection feature for walking gait is the specific force at the ankle. The relationship between the shin-mounted IMU measurements and the specific force at the ankle can be expressed as follows:

$$\boldsymbol{f}_{ankle}^b = \boldsymbol{f}^b + \left(\boldsymbol{\omega}^b \times\right)\left(\boldsymbol{\omega}^b \times\right) \boldsymbol{C}_s^b \boldsymbol{l}^s + \left(\dot{\boldsymbol{\omega}}^b \times\right) \boldsymbol{C}_s^b \boldsymbol{l}^s \quad (3)$$

where $\boldsymbol{f}^b$ and $\boldsymbol{\omega}^b$ are the specific force and angle rate come from the shin-mounted IMU, $\boldsymbol{l}^s = \begin{bmatrix} 0 & 0 & Dis \end{bmatrix}^T$ is the position vector from the IMU measurement center to the ankle in the shin frame ($s$-frame), $Dis$ is the distance from IMU to ankle, which can be measured with a tape measure, $\dot{\boldsymbol{\omega}}^b$ is the angular acceleration in the $b$-frame, and $(\cdot)\times$ is the skew-symmetric matrix of the vector.

When the foot contacts the ground, the acceleration at the ankle should be zero. Based on this principle, we employ the generalized likelihood ratio test (GLRT) method to establish a zero-velocity detection criterion.

$$\frac{1}{2N+1} \sum_{i=k-N}^{k+N} \left\| \boldsymbol{f}_{ankle,i}^b - g\frac{\overline{\boldsymbol{f}}_{ankle}^b}{\left\|\overline{\boldsymbol{f}}_{ankle}^b\right\|} \right\| \leq \boldsymbol{\gamma}_{W1} \quad (4)$$

where $\boldsymbol{f}_{ankle,i}^b$ is the estimated specific force at the ankle computed via Eq. 3, $\overline{\boldsymbol{f}}_{ankle}^b$ is the average specific force at
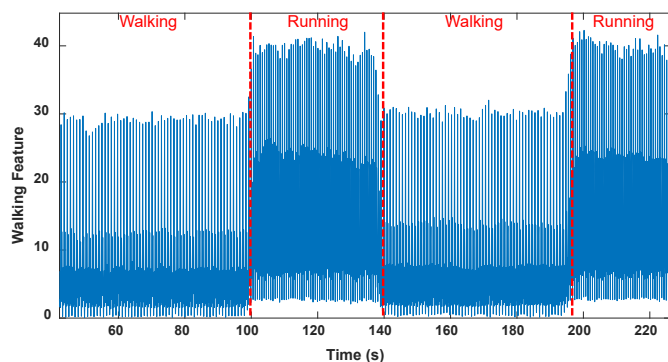
Fig. 3: The difference between walking feature in walking and running gaits.

the ankle, $g = 9.8 m/s^2$ is the gravitational acceleration on Earth, $2N + 1$ is the length of the sampling window, $\gamma_{W1}$ is a predetermined empirical threshold, and $\|\cdot\|$ denotes the Euclidean norm (i.e., the $L2$ norm). To further refine the accuracy of the ground contact interval, the following equation is utilized to impose additional constraints:

$$Max\left(\left\|\boldsymbol{f}_{ankle}^b\right\|_{k-N:k+N}\right) - Min\left(\left\|\boldsymbol{f}_{ankle}^b\right\|_{k-N:k+N}\right) \leq \gamma_{W2} \tag{5}$$

where $\gamma_{W2}$ is a predetermined empirical threshold.

Our previously published results demonstrate that the zero-velocity detection feature, as described in Eq. 4, is adaptable to various gait patterns, including normal, sideways, and diagonal walking. However, as illustrated in Fig. 3, the dynamic characteristics of running differ significantly from those of walking. Running is characterized by much shorter contact intervals, making the feature specified in Eq. 4 unsuitable for zero-velocity detection during running gait.

### C. Zero-Velocity Detection during Running

As described in Section II, the dynamics of lower limbs in the running gait resemble a pogo stick. This characteristic invalidates the assumption that the ankle's acceleration is zero. However, during the running gait, when the foot supports the body, the lower limbs straighten completely. During this contact period, the centripetal acceleration along the shin, pointing towards the waist, approaches zero. Simultaneously, the lower limbs maintain a fixed-point rotation around the foot's contact point with the ground. Additionally, the body's lateral acceleration, or tangential acceleration, remains relatively stable, ensuring human balance.

The centripetal acceleration and tangential acceleration in the shin frame ($s$-frame) can be expressed as:

$$\begin{cases} \boldsymbol{a}_{Shin,C} = \left((\boldsymbol{\omega}^b\times)(\boldsymbol{\omega}^b\times)\boldsymbol{C}_s^b\boldsymbol{l}^s\right)_3 \\ \boldsymbol{a}_{Shin,T} = \left((\dot{\boldsymbol{\omega}}^b\times)\boldsymbol{C}_s^b\boldsymbol{l}^s\right)_2 \end{cases} \tag{6}$$

where $\boldsymbol{a}_{Shin,C}$ represents the component of centripetal acceleration aligned along the shin pointing to the waist, $\boldsymbol{a}_{Shin,T}$ represents the component of the lateral acceleration of the human body, $(\cdot)_2$ represents the second component of the vector.

Fig. 4 illustrates the waveforms of $\boldsymbol{a}_{Shin,C}$ (centripetal acceleration) and $\boldsymbol{a}_{Shin,T}$ (tangential acceleration) during running gait. The centripetal acceleration $\boldsymbol{a}_{Shin,C}$ remains close to zero whether the foot is in a zero-velocity state or not, although the relative change is slower when the foot is in a zero-velocity state. Conversely, $\boldsymbol{a}_{Shin,T}$ exhibits a clearer waveform; however, its tangential acceleration is influenced by individual exercise habits and physical condition, showing no consistent pattern in absolute values. Therefore, $\boldsymbol{a}_{Shin,C}$ is chosen as the primary feature for zero-velocity detection in running gait, with $\boldsymbol{a}_{Shin,T}$ serving as an auxiliary feature to mitigate false detections. The specific criteria for zero-velocity detection in running gait are as follows:

$$\begin{cases} \boldsymbol{a}_{Shin,C} > \boldsymbol{\gamma}_{R1} \\ \boldsymbol{a}_{Shin,T} < \boldsymbol{\gamma}_{R2} \end{cases} \tag{7}$$

where $\boldsymbol{\gamma}_{R1}$ and $\boldsymbol{\gamma}_{R2}$ are given empirical thresholds respectively.
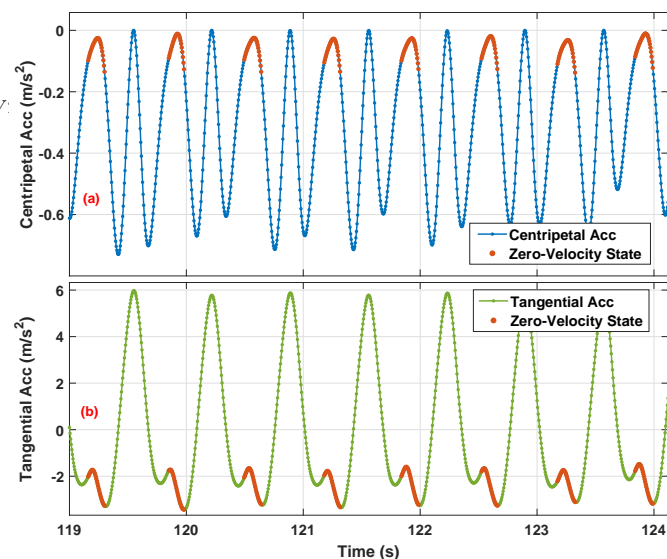


Fig. 4: The waveforms of $\boldsymbol{a}_{Shin,C}$ and $\boldsymbol{a}_{Shin,T}$ in running gait

Furthermore, during normal walking gait, the zero-velocity intervals identified using running features are a subset of those identified using walking features, as illustrated in Fig. 5. This indicates that running-related features are also applicable to typical walking gait. Consequently, even if the walking gait is misclassified as a running gait, it will not significantly impact the positioning performance of the proposed algorithm. More importantly, incorporating walking features aims to enhance the adaptability of the zero-velocity detection algorithm to abnormal gait patterns, such as sideways walking.

### IV. SHIN-MOUNTED INERTIAL NAVIGATION SYSTEM

The robust zero-velocity detector is crucial for maintaining the effectiveness of zero update technology in complex gait patterns. Building on this, the extended Kalman filter (EKF) is employed to fuse the inertial navigation algorithm, resulting
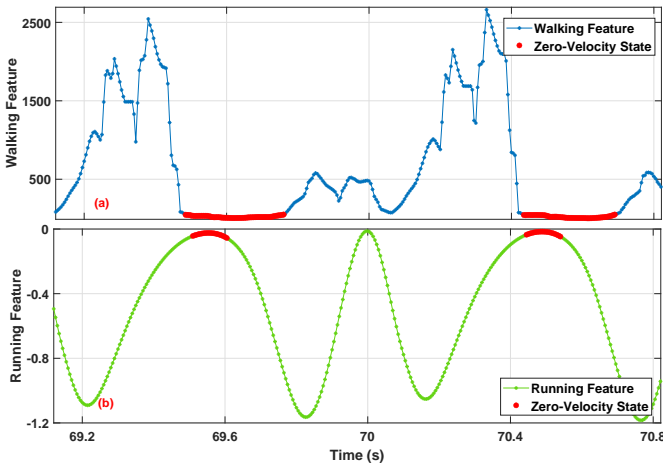
Fig. 5: Zero-velocity intervals detected in walking gait using walking feature and running feature.

in a robust pedestrian dead reckoning system known as Shin-INS-Fusion. Fig. 4 illustrates the algorithm flow of Shin-INS-Fusion. In this system, the inertial navigation algorithm integrates measurements from the gyroscope and accelerometer to estimate the sensor's attitude, velocity, and position at each epoch. During both walking and running, the zero-position incremental update technology, based on lever arm compensation, ensures regular correction of inertial navigation velocity errors. Additionally, during the stationary phase, the zero-velocity update technology (ZUPT) prevents the inertial navigation error from diverging.
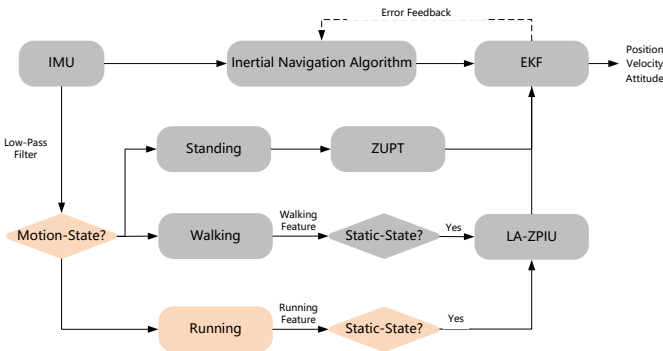


Fig. 6: Algorithm flow of Shin-INS-Fusion.

### A. Inertial Navigation Algorithm

The strapdown inertial navigation algorithm used in this paper omits minor error correction terms such as the Earth's rotation and the paddling effect. This simplification is due to the inherent characteristics of MEMS IMUs, which include large initial bias and high noise levels; thus, minor error correction terms do not significantly enhance positioning performance. The simplified INS mechanization algorithm is

detailed as follows [20]:

$$
\begin{cases}
\boldsymbol{r}_k^n = \boldsymbol{r}_{k-1}^n + \boldsymbol{v}_k^n \Delta t_k \\
\boldsymbol{v}_k^n = \boldsymbol{v}_{k-1}^n + \boldsymbol{C}_{b,k}^n \left( \Delta \boldsymbol{v}_k^b + \dfrac{\Delta \boldsymbol{\theta}_k^b \times \Delta \boldsymbol{v}_k^b}{2} \right) + \boldsymbol{g}^n \Delta t_k \\
\boldsymbol{C}_{b,k}^n = \boldsymbol{C}_{b,k-1}^n \left[ \boldsymbol{I} + \Delta \boldsymbol{\theta}_k^b + \dfrac{\Delta \boldsymbol{\theta}_{k-1}^b \times \Delta \boldsymbol{\theta}_k^b}{12} \right]
\end{cases} \tag{8}
$$

where $\boldsymbol{r}^n$ and $\boldsymbol{v}^n$ are the position and velocity vectors in the $n$-frame, respectively; $\boldsymbol{C}_b^n$ is the transformation matrix from the $b$-frame to the $n$-frame; $\boldsymbol{g}^n = \begin{bmatrix} 0, 0, 9.8 \end{bmatrix}^T$ is Earth's gravity vector; $\Delta \boldsymbol{v}_k^b = \left( \tilde{\boldsymbol{f}}_k^b - \boldsymbol{b}_{f,k} \right) \Delta t_k$ is the velocity increment in the $b$-frame; $\tilde{\boldsymbol{f}}^b$ and $\boldsymbol{b}_f$ are the specific force and bias of the accelerometer, respectively; $\Delta \boldsymbol{\theta}_k^b = \left( \tilde{\boldsymbol{\omega}}_k^b - \boldsymbol{b}_{\omega,k} \right) \Delta t_k$ is the angle increment in the $b$-frame; $\tilde{\boldsymbol{\omega}}^b$ and $\boldsymbol{b}_g$ are the angle rate and bias of the gyroscope, respectively; $\Delta t_k = t_k - t_{k-1}$ is the time interval between the $(k-1)$-th and $k$-th epochs; and "$\times$" is the cross-product form of a vector.

### B. Extended Kalman Filter

The error state extended Kalman filter (ES-EKF) is employed to fuse inertial navigation and motion constraints. The error state is defined as the difference between the estimated value and the true value. An 18-dimensional error navigation state is used, which includes the following components:

$$
\boldsymbol{X} = \begin{bmatrix} \delta \boldsymbol{r}^n & \delta \boldsymbol{v}^n & \boldsymbol{\phi} & \delta \boldsymbol{b}_\omega & \delta \boldsymbol{b}_f & \delta \boldsymbol{l}^b \end{bmatrix}^T \tag{9}
$$

where $\delta \boldsymbol{r}^n$ and $\delta \boldsymbol{v}^n$ are the position and velocity error vector in the $n$-frame, respectively; $\boldsymbol{\phi}$ is the attitude error vector; $\delta \boldsymbol{b}_\omega$ and $\delta \boldsymbol{b}_f$ are the gyro and accelerometer bias error vector, respectively, modeled as first-order Markov processes; $\delta \boldsymbol{l}_b$ is the lever arm error vector in the $b$-frame. The continuous system error propagation model is given by [21]:

$$
\dot{\boldsymbol{X}} = \boldsymbol{F} \boldsymbol{X} + \boldsymbol{G} \boldsymbol{W} \tag{10}
$$

$$
\boldsymbol{F} = \begin{bmatrix}
\boldsymbol{0}_3 & \boldsymbol{I}_3 & \boldsymbol{0}_3 & \boldsymbol{0}_3 & \boldsymbol{0}_3 & \boldsymbol{0}_3 \\
\boldsymbol{0}_3 & \boldsymbol{0}_3 & \boldsymbol{f}^n \times & \boldsymbol{C}_b^n & \boldsymbol{0}_3 & \boldsymbol{0}_3 \\
\boldsymbol{0}_3 & \boldsymbol{0}_3 & \boldsymbol{0}_3 & \boldsymbol{0}_3 & -\boldsymbol{C}_b^n & \boldsymbol{0}_3 \\
\boldsymbol{0}_3 & \boldsymbol{0}_3 & \boldsymbol{0}_3 & \boldsymbol{I}_3 \left( -1/\boldsymbol{\tau}_{b_f} \right) & \boldsymbol{0}_3 & \boldsymbol{0}_3 \\
\boldsymbol{0}_3 & \boldsymbol{0}_3 & \boldsymbol{0}_3 & \boldsymbol{0}_3 & \boldsymbol{I}_3 \left( -1/\boldsymbol{\tau}_{b_\omega} \right) & \boldsymbol{0}_3 \\
\boldsymbol{0}_3 & \boldsymbol{0}_3 & \boldsymbol{0}_3 & \boldsymbol{0}_3 & \boldsymbol{0}_3 & \boldsymbol{0}_3
\end{bmatrix} \tag{11}
$$

$$
\boldsymbol{G} = \begin{bmatrix}
\boldsymbol{0}_3 & \boldsymbol{0}_3 & \boldsymbol{0}_3 & \boldsymbol{0}_3 & \boldsymbol{0}_3 \\
\boldsymbol{C}_b^n & \boldsymbol{0}_3 & \boldsymbol{0}_3 & \boldsymbol{0}_3 & \boldsymbol{0}_3 \\
\boldsymbol{0}_3 & -\boldsymbol{C}_b^n & \boldsymbol{0}_3 & \boldsymbol{0}_3 & \boldsymbol{0}_3 \\
\boldsymbol{0}_3 & \boldsymbol{0}_3 & \boldsymbol{I}_3 & \boldsymbol{0}_3 & \boldsymbol{0}_3 \\
\boldsymbol{0}_3 & \boldsymbol{0}_3 & \boldsymbol{0}_3 & \boldsymbol{I}_3 & \boldsymbol{0}_3 \\
\boldsymbol{0}_3 & \boldsymbol{0}_3 & \boldsymbol{0}_3 & \boldsymbol{0}_3 & \boldsymbol{I}_3
\end{bmatrix}, \quad
\boldsymbol{W} = \begin{bmatrix}
\boldsymbol{w}_f \\
\boldsymbol{w}_\omega \\
\boldsymbol{w}_{b_f} \\
\boldsymbol{w}_{b_\omega} \\
\boldsymbol{w}_{l^b}
\end{bmatrix} \tag{12}
$$

where $\boldsymbol{F}$ is the dynamic transition matrix, $\boldsymbol{G}$ is the noise coefficient matrix, $\boldsymbol{W}$ is the system noise, $\boldsymbol{I}_3$ is a 3-dimensional identity matrix, $\Delta t$ is the time interval between adjacent epochs, $\boldsymbol{f}^n = \boldsymbol{C}_b^n \left( \tilde{\boldsymbol{f}}^b - \boldsymbol{b}_f \right)$ is the accelerometer observation in the $n$-frame, $\boldsymbol{C}_b^n$ is the direction cosine matrix from the $b$-frame to the $n$-frame, $\tau_{b_\omega}$ and $\tau_{b_f}$ are the time constants for the

gyro and accelerometer bias error models, $\boldsymbol{w}_f$ and $\boldsymbol{w}_\omega$ are the noise associated with the accelerometer and gyroscope outputs, respectively, $\boldsymbol{w}_{b_f}$ and $\boldsymbol{w}_{b_\omega}$ are the driving white noise for the accelerometer and gyroscope bias error models, respectively, and $\boldsymbol{w}_{l_b}$ is the white noise for the lever arm model.

Due to the small sampling interval of the MEMS IMU ( $\Delta t = 0.005s$ ) and $\boldsymbol{F}_k \Delta t \ll \boldsymbol{I}$ , the discrete system state model is derived as follows [22]:

$$
\begin{cases}
\boldsymbol{X}_k = \boldsymbol{\Phi}_{k,k-1} \boldsymbol{X}_{k-1} + \boldsymbol{w}_{k-1} \\
\boldsymbol{\Phi}_{k,k-1} = \boldsymbol{exp}\left[\boldsymbol{F}_{k-1}\Delta t\right] \approx \boldsymbol{I}_{18} + \boldsymbol{F}_k \Delta t \\
\boldsymbol{Q}_k \approx \frac{\Delta t}{2}\left(\boldsymbol{\Phi}_{k,k-1}\boldsymbol{G}_{k-1}\boldsymbol{Q}\boldsymbol{G}_{k-1}^T\boldsymbol{\Phi}_{k,k-1}^T + \boldsymbol{G}_k\boldsymbol{Q}\boldsymbol{G}_k^T\right)
\end{cases}
\tag{13}
$$

where $\boldsymbol{\Phi}_{k,k-1}$ is the discrete transform matrix, $\boldsymbol{Q}$ is the covariance matrix of the discrete system noise $\boldsymbol{w}_{k-1}$, and $\boldsymbol{exp}\left(\cdot\right)$ denotes the exponential function.

### C. Zero Observation Model

When a pedestrian's foot touches the ground, there's a point at which the foot's velocity is zero. However, due to the complexity, diversity, and irregularity of pedestrian gait, it is challenging to determine the precise position of the foot's contact point using only a shin-mounted IMU. To address this, we construct constraints based on the objective observation that the ankle position changes minimally during the foot-ground contact period. The observation equation for zero position increment is expressed as [9]:

$$
\begin{aligned}
\delta\boldsymbol{z}_{\Delta r^n} \approx & \sum_{i=1}^{N} \boldsymbol{I}_3 \Delta t_i \delta\boldsymbol{v}^n + \sum_{i=1}^{N}\left(\boldsymbol{C}_{b,i}^n \boldsymbol{\omega}_i^b \times \boldsymbol{l}_i^b\right) \times \Delta t_i \boldsymbol{\phi} \\
& - \sum_{i=1}^{N} \boldsymbol{C}_{b,i}^n \left(\boldsymbol{l}_i^b \times\right) \Delta t_i \delta\boldsymbol{b}_\omega + \sum_{i=1}^{N} \boldsymbol{C}_{b,i}^n \left(\boldsymbol{\omega}_i^b \times\right) \Delta t_i \delta\boldsymbol{l}^b \\
& - \boldsymbol{n}_{\Delta r^n}
\end{aligned}
\tag{14}
$$

where $N$ is the epoch number within the zero velocity interval $[t_{k-1}, t_k]$, $\Delta t_i$, $\boldsymbol{C}_{b,i}^n$, $\boldsymbol{\omega}_i^b$ and $\boldsymbol{l}_i^b$ are the time interval, direction cosine matrix, angular rate and lever arm of the $i$-th epoch in the window, and $\boldsymbol{n}_{\Delta r^n}$ is the observation noise.

Since the lever arm $\boldsymbol{l}^b$ is observable only when the pedestrian is in motion, ZUPT is used instead of zero position increment update when the pedestrian is stationary. This approach ensures the stability of the lever arm $\boldsymbol{l}^b$ state estimation. The observation equation for ZUPT is as follows:

$$
\begin{aligned}
\delta\boldsymbol{z}_{v^n} &= \hat{\boldsymbol{v}}^n - \tilde{\boldsymbol{v}}^n \\
&= \hat{\boldsymbol{v}}^n - \left(\begin{bmatrix} 0 & 0 & 0 \end{bmatrix}^T + \boldsymbol{n}_{v^n}\right) \\
&\approx \delta\boldsymbol{v}^n - \boldsymbol{n}_{v^n}
\end{aligned}
\tag{15}
$$

where $\boldsymbol{n}_{v^n}$ is zero-velocity observation noise. In addition, when ZUPT is available, the zero integral heading rate (ZIHR) can also be used to control the INS heading drift error. For details, please refer to [9].

### V. EXPERIMENTAL RESULT

### A. Test Description

This section evaluates the positioning performance of the proposed method under complex pedestrian gait conditions using real-world pedestrian data. Fig. 5 illustrates the equipment

setup. Inertial sensors are mounted on the heels and calves of the test subjects, while a GNSS antenna is placed on top of the head, and the GNSS receiver is carried in a backpack. The inertial sensor modules, developed by the WHU-i2Nav team, transmit their respective timestamps to a smartphone via Bluetooth for time synchronization. The inertial sensors feature a bias instability of 10 °/h and 0.2 mg, and white noise levels of 0.24 $°/\sqrt{\text{h}}$ and 0.06 $\text{m/s}/\sqrt{\text{h}}$. Since the test environment is an open sky area, GNSS provides centimeter-level positioning accuracy.

The positioning performance of three distinct schemes was evaluated, namely: 1) **Foot-INS**: This scheme incorporates ZUPT and ZIHR, the specific algorithm can be found in [22]. 2) **Foot-INS-Robust**: This scheme integrates zero velocity detection suitable for complex environments into Foot-INS [15]. 3) **Shin-INS-Fusion**: The solution proposed in this paper.

The test data covers both running and walking gaits. The running gait involves different movement speeds, and the trajectory shapes include straight lines and arcs. To verify the stability of the algorithm when switching between various walking states, the test dataset contains continuous transitions between running and walking gaits. For ease of evaluation, the initial 10-meter trajectory inferred by each algorithm is aligned with the reference trajectory.



Fig. 7: The relative position of the experimental equipments on the human body.

### B. Running gait testing on straight trajectories

A total of 24 tests were conducted on a 100-meter long straight track, involving five participants who were instructed to run at varying speeds. The trajectories estimated by the Foot-INS, Foot-INS-Robust, and Shin-INS-Fusion algorithms are depicted in Fig. 8. Compared to the other methods, the proposed method estimates user trajectories more continuously and with higher accuracy. To evaluate the distance estimation accuracy of each algorithm, we computed the endpoint position error for each experimental setup. Fig. 9 shows the endpoint position errors of the estimated 100-meter straight trajectories using the three positioning schemes in 24 tests. The Root Mean Square (RMS) errors for the endpoint positions of Foot-INS, Foot-INS-Robust, and Shin-INS-Fusion are 10.11

This article has been accepted for publication in IEEE Sensors Journal. This is the author's version which has not been fully edited and content may change prior to final publication. Citation information: DOI 10.1109/JSEN.2025.3533138

AUTHOR *et al.*: PREPARATION OF PAPERS FOR IEEE TRANSACTIONS AND JOURNALS (FEBRUARY 2017)                                                                                   7

m, 7.55 m, and 2.24 m, respectively. Foot-INS exhibited the lowest positioning accuracy and even failed to work properly in some test cases, likely due to its reliance on fixed thresholds and difficulty in adapting to running gaits. In contrast, Shin-INS-Fusion demonstrated superior positioning performance compared to Foot-INS-Robust. This improvement may be attributed to the proposed method's ability to obtain more reliable zero-velocity intervals under mixed gaits and the reduced impact on the shin during both walking and running gaits, leading to lower dynamic errors in the MEMS-IMU. Additionally, Shin-INS-Fusion employs a position incremental update method, which mitigates the impact of gait discrimination errors on positioning performance.
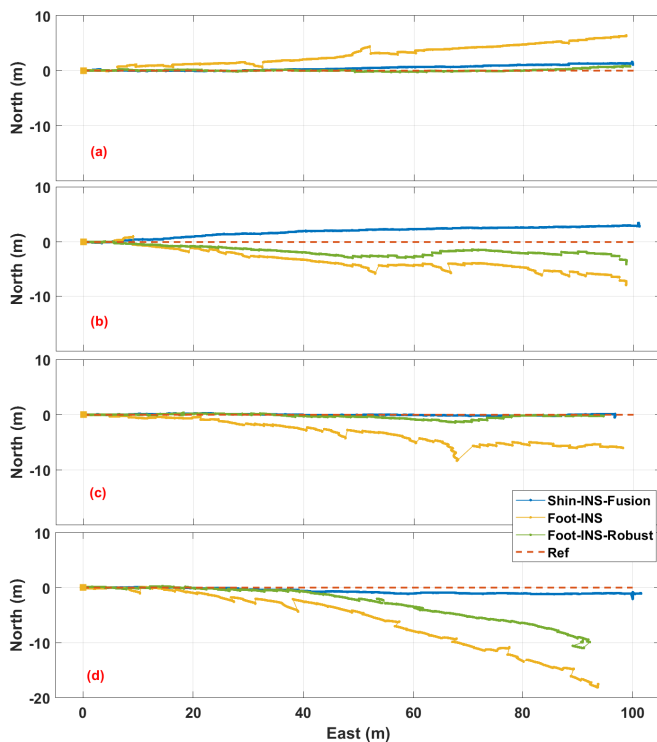


Fig. 8: The estimated 100-m straight trajectories using 3 positioning schemes in 4 tests.
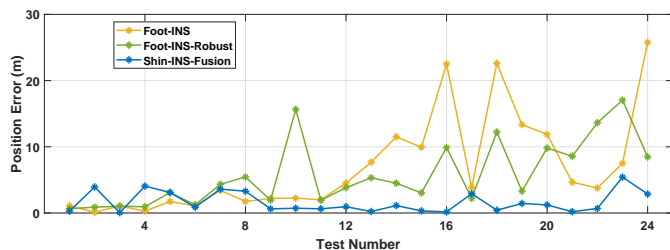


Fig. 9: Endpoint position errors of the estimated 100-m straight trajectories using 3 positioning schemes in 24 tests.

## C. Running gait testing on straight and curved trajectories

We conducted 18 tests on a sports track, including three types: slow, fast, and variable speeds. Specifically, the slow

speed ranged from 2.4-2.8 $m/s$, the fast speed ranged from 3.4-4.0 $m/s$, and the variable speed involved slow running on the curved sections and fast running on the straight sections of the track. Each type consisted of six experiments, completed by four participants, with each participant performing at least one experiment. Fig. 10 shows the trajectories estimated using 3 positioning schemes in 4 tests at different running speeds, where subfigures (a) and (b) represent fast speeds, (c) represents slow speed, and (d) represents mixed speed. Table I statistics the root mean square (RMS) of position errors for trajectories estimated using 3 different positioning schemes at different running speeds. The RMS of the position errors of Foot-INS, Foot-INS-Robust, and Shin-INS-Fusion are 17.66 m, 11.21 m, and 7.66 m in the slow running gait, 27.52 m, 22.69 m, and 8.38 m in the fast running gait, and 25.96 m, 12.05 m, and 6.70 m in the variable speed running gait. Compared with Foot-INS and Foot-INS-Robust, Shin-INS-Fusion reduces the positioning error by 56.62% and 31.66% in low-speed running gait, 69.54% and 63.06% in fast-speed running gait, and 74.19% and 44.39% in variable-speed running gait.

Compared to the traditional Foot-INS, Foot-INS-Robust benefits from zero-velocity detection technology based on an adaptive threshold. This approach reduces sensitivity to variations in zero-velocity detection features due to changes in the user's gait. While Foot-INS-Robust shows stable performance in slow and variable-speed running gaits, its accuracy significantly drops during fast-speed running. This decline occurs because there is often no clear zero-velocity interval for the heel during high-speed running, blurring the distinction between zero-velocity and non-zero-velocity states. This results in decreased accuracy for zero-velocity detection methods reliant on adaptive thresholds. In contrast, Shin-INS-Fusion maintains consistent positioning performance across different running speeds. This consistency is attributed to the improved reliability of zero-velocity detection features derived from the shin-mounted IMU, which exhibit better adaptability to varying running speeds. The proposed method utilizes these features to provide a more reliable zero-velocity detector. Additionally, Shin-INS-Fusion adaptively estimates the relative position from the shin-mounted IMU to the foot contact point, mitigating the adverse effects of gait changes on positioning accuracy.

TABLE I: Root mean square (RMS) of position errors for trajectories estimated using 3 different positioning schemes at different running speeds.

| Test | Foot-INS | | | Foot-INS-Robust | | | Shin-INS-Fusion | | |
|------|------|------|----------|------|------|----------|------|------|----------|
| | Slow | Fast | Variable | Slow | Fast | Variable | Slow | Fast | Variable |
| 1 | 31.6 | 24.84 | 31.14 | 21.89 | 24.96 | 7.8 | 12.39 | 9.52 | 8.37 |
| 2 | 22.03 | 35.93 | 36.29 | 12.21 | 9.8 | 17.6 | 15.58 | 4.43 | 13.52 |
| 3 | 10.04 | 25.14 | 7.39 | 9.69 | 18.54 | 4.87 | 5.64 | 4.05 | 6.13 |
| 4 | 26.73 | 19.68 | 60.39 | 6.16 | 27.76 | 22.24 | 5.84 | 6.75 | 6.97 |
| 5 | 12.06 | 48.5 | 12.55 | 12.51 | 43.64 | 11.95 | 4.45 | 12.12 | 3.83 |
| 6 | 3.53 | 11.05 | 7.98 | 4.83 | 11.46 | 7.82 | 2.08 | 13.4 | 1.38 |
| Mean | 17.66 | 27.52 | 25.96 | 11.21 | 22.69 | 12.05 | **7.66** | **8.38** | **6.70** |
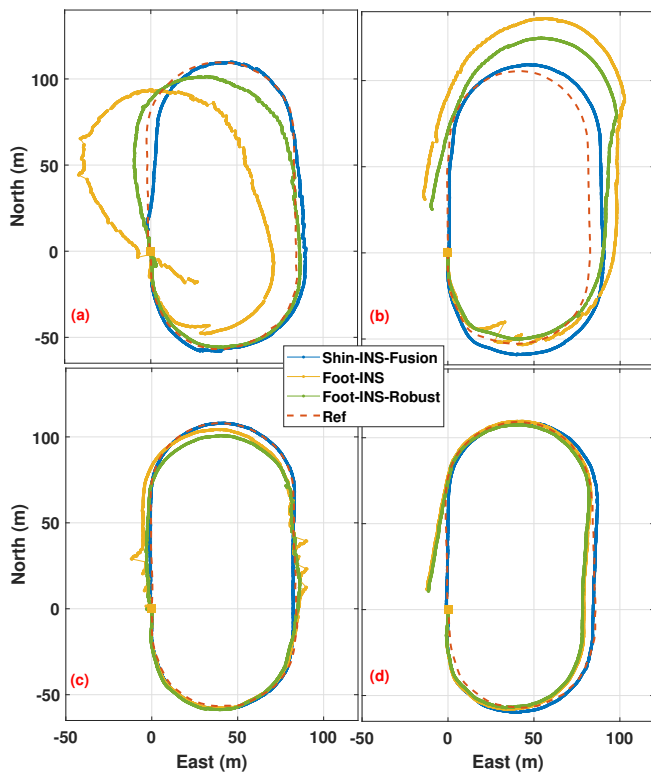
Fig. 10: Trajectories estimated using 3 positioning schemes in 4 tests at different running speeds. (subfigures (a) and (b) represent fast speeds, (c) represents slow speed, and (d) represents mixed speed)

### D. Mixed gait testing on straight and curved trajectories

We conducted 4 mixed gait tests on a sports field track, with each test corresponding to one participant. In each test, the participant ran on the straight sections and walked on the curved sections, covering a total distance of approximately 400 meters. Fig. 11 illustrates the estimated trajectories using 3 positioning schemes in 4 mixed gait tests. Table II summarizes the RMS of position errors for trajectories estimated using 3 different positioning schemes with mixed gaits. The average RMS of position errors for Foot-INS, Foot-INS-Robust, and Shin-INS-Fusion are 13.74 m, 6.94 m, and 4.37 m, respectively. Compared with Foot-INS and Foot-INS-Robust, Shin-INS-Fusion reduces the positioning error by 68.19% and 37.03%.

In mixed gaits, where running often occurs at lower speeds, the Foot-INS method can maintain relatively consistent zero-velocity detection by using a larger threshold. This approach helps ensure the continuity of the estimated trajectory. However, employing a larger threshold can lead to erroneous zero-velocity updates (ZUPT), resulting in significant scaling inaccuracies in the trajectory estimates produced by Foot-INS. In contrast, the Foot-INS-Robust method does not rely on a fixed threshold, thereby avoiding the scale issues associated with Foot-INS. As a result, Foot-INS-Robust performs more stably across mixed jogging and walking scenarios. The Shin-INS-Fusion scheme excels by integrating a comprehensive ground contact interval detection method tailored for both

running and walking gaits. This approach effectively identifies zero-velocity intervals in diverse gaits, resulting in the highest positioning accuracy among the three schemes.
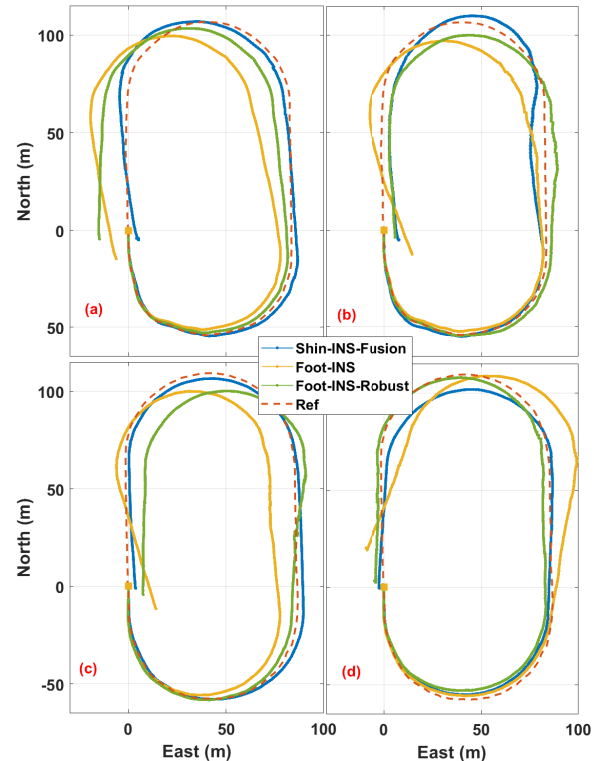


Fig. 11: Trajectories estimated using 3 positioning schemes with mixed gaits.

TABLE II: Root mean square (RMS) of position errors for trajectories estimated using 3 different positioning schemes with mixed gaits.

| Test | Foot-INS | Foot-INS-Robust | Shin-INS-Fusion |
|------|----------|-----------------|-----------------|
| 1 | 17.06 | 9.53 | 5.80 |
| 2 | 12.87 | 5.86 | 5.60 |
| 3 | 11.46 | 8.35 | 1.50 |
| 4 | 13.57 | 4.02 | 4.57 |
| Mean | 13.74 | 6.94 | **4.37** |

### E. Discussion

The accuracy of zero-velocity detection is crucial, as it directly impacts the positioning performance of Shin-INS-Fusion. In this paper, we propose a novel zero-velocity detection feature tailored for running gait, as illustrated in Eq. 6 and Eq. 7. Consequently, it is essential to evaluate the accuracy of zero-velocity detection. Due to the absence of a reference system that can provide true zero-velocity intervals across such an extensive test scene, we utilize manually labeled steps as our reference. We meticulously counted the actual number of steps and the number of steps detected by the algorithm, which includes false detections and missed detections, for each running dataset. From these counts, we calculated precision

This article has been accepted for publication in IEEE Sensors Journal. This is the author's version which has not been fully edited and content may change prior to final publication. Citation information: DOI 10.1109/JSEN.2025.3533138

AUTHOR *et al.*: PREPARATION OF PAPERS FOR IEEE TRANSACTIONS AND JOURNALS (FEBRUARY 2017)                                              9
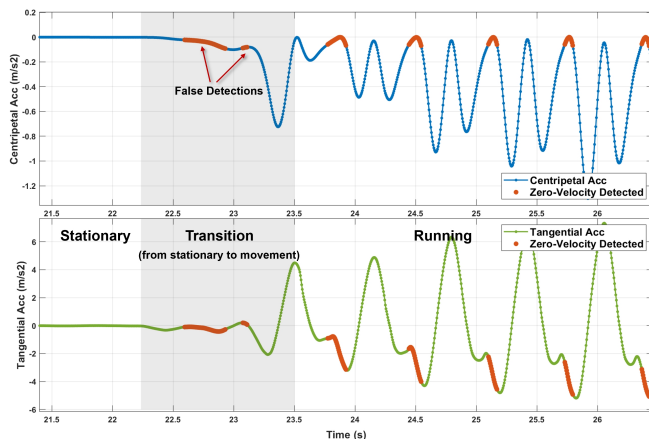
Fig. 12: Possible false detections during the transition from stationary to movement.

TABLE III: The precision and recall of step detection under different running speeds.

| Test | Slow | | Fast | | Variable | |
|---|---|---|---|---|---|---|
| | Precision | Recall | Precision | Recall | Precision | Recall |
| 1 | 100.00% | 100.00% | 99.46% | 100.00% | 98.77% | 100.00% |
| 2 | 99.13% | 100.00% | 99.46% | 100.00% | 98.77% | 100.00% |
| 3 | 100.00% | 99.17% | 99.44% | 100.00% | 100.00% | 99.48% |
| 4 | 99.59% | 99.59% | 100.00% | 99.44% | 98.97% | 100.00% |
| 5 | 99.51% | 100.00% | 100.00% | 100.00% | 99.52% | 100.00% |
| 6 | 100.00% | 100.00% | 100.00% | 100.00% | 99.53% | 100.00% |
| Mean | 99.70% | 99.79% | 99.73% | 99.91% | 99.26% | 99.91% |

(the ratio of true steps among those detected by the algorithm) and recall (the ratio of true steps correctly identified by the algorithm). Table III summarizes the precision and recall of step detection for each dataset across different running speeds. The average precision and recall for slow running, fast running, and variable-speed running are 99.70%/99.79%, 99.73%/99.91%, and 99.26%/99.91%, respectively. The proposed features in the running gait exhibit distinct peaks and valleys, making them readily distinguishable. However, there are some instances of false detections and missed detections during the transition from static to running gait, as depicted in 4. This phenomenon occurs because the zero-velocity detection feature lacks stable characteristics during the gait transition phase. Nonetheless, the impact of false detections in the zero-velocity interval during this transition is minimal on positioning performance, as the foot remains close to the ground at this time. Furthermore, the proposed zero position increment update effectively mitigates this influence.

## VI. CONCLUSION

This paper proposes a shin-mounted INS designed for pedestrian walking and running gaits. By classifying pedestrian gaits and developing zero-velocity detection features based on these classifications, the method achieves reliable zero-velocity detection in mixed walking and running gaits. Building on this, the method incorporates zero-position increment updates with lever arm compensation and zero-velocity update technology to ensure accurate pedestrian positioning in complex gait scenarios. Experimental validation demonstrates that the proposed approach effectively detects foot-ground contact periods across a range of slow (2.4-2.8 m/s), fast (3.4-4.0 m/s), and mixed slow-fast speeds. It also performs well in mixed running and walking gaits. Compared to traditional Foot-INS and the Foot-INS-Robust methods, which rely on adaptive thresholds, the proposed method enhances positioning accuracy by over 60% and 30%, respectively.

This paper examines the positioning performance of Shin-INS across various complex gaits, including walking, running, and mixed gait speeds. However, its performance in more demanding gaits, such as jumping and crawling, and in challenging terrains like rugged mountainous environments, remains to be explored. Future research will aim to evaluate Shin-INS's positioning capabilities in extreme scenarios and diverse gait conditions to ensure its effectiveness in critical applications such as firefighting and rescue operations.

## REFERENCES

[1] R. Chen and L. Chen, "Smartphone-based indoor positioning technologies," *Urban informatics*, pp. 467–490, 2021.
[2] N. El-Sheimy and Y. Li, "Indoor navigation: State of the art and future trends," *Satell. Navig.*, vol. 2, no. 1, pp. 1–23, 2021.
[3] X. Cao, Y. Zhuang, X. Yang, X. Sun, and X. Wang, "A universal wi-fi fingerprint localization method based on machine learning and sample differences," *Satell. Navig.*, vol. 2, no. 1, pp. 1–15, 2021.
[4] J. Chen, B. Zhou, S. Bao, X. Liu, Z. Gu, L. Li, Y. Zhao, J. Zhu, and Q. Li, "A data-driven inertial navigation/bluetooth fusion algorithm for indoor localization," *IEEE Sens. J.*, vol. 22, no. 6, pp. 5288–5301, 2021.
[5] B. Van Herbruggen, B. Jooris, J. Rossey, M. Ridolfi, N. Macoir, Q. Van den Brande, S. Lemey, and E. De Poorter, "Wi-pos: A low-cost, open source ultra-wideband (uwb) hardware platform with long range sub-ghz backbone," *Sensors*, vol. 19, no. 7, p. 1548, 2019.
[6] J. Kuang, T. Li, and X. Niu, "Magnetometer bias insensitive magnetic field matching based on pedestrian dead reckoning for smartphone indoor positioning," *IEEE Sens. J.*, 2021.
[7] J. Kuang, T. Li, Q. Chen, B. Zhou, and X. Niu, "Consumer-grade inertial measurement units enhanced indoor magnetic field matching positioning scheme," *IEEE Trans. Instrum. Meas.*, vol. 72, pp. 1–14, 2022.
[8] J. Kuang, X. Niu, and X. Chen, "Robust pedestrian dead reckoning based on mems-imu for smartphones," *Sensors*, vol. 18, no. 5, p. 1391, 2018.
[9] J. Kuang, D. Xia, T. Liu, Q. Chen, and X. Niu, "Shin-ins: A shin-mounted imu-based inertial navigation system for pedestrian," *IEEE Sens. J.*, vol. 23, no. 21, pp. 25 760–25 769, 2023.
[10] I. Skog, P. Handel, J. O. Nilsson, and J. Rantakokko, "Zero-Velocity Detection—An Algorithm Evaluation," *IEEE Trans. Biomed. Eng.*, vol. 57, no. 11, pp. 2657–2666, Nov. 2010.
[11] Z. Wang, H. Zhao, S. Qiu, and Q. Gao, "Stance-phase detection for zupt-aided foot-mounted pedestrian navigation system," *IEEE-ASME Trans. Mechatron.*, vol. 20, no. 6, pp. 3170–3181, 2015.
[12] J. Wahlström, I. Skog, F. Gustafsson, A. Markham, and N. Trigoni, "Zero-velocity detection—a bayesian approach to adaptive thresholding," *IEEE Sens. Lett.*, vol. 3, no. 6, pp. 1–4, 2019.
[13] B. Wagstaff, V. Peretroukhin, and J. Kelly, "Robust data-driven zero-velocity detection for foot-mounted inertial navigation," *IEEE Sens. J.*, vol. 20, no. 2, pp. 957–967, 2020.
[14] Y. Kone, N. Zhu, and V. Renaudin, "Zero velocity detection without motion pre-classification: Uniform ai model for all pedestrian motions (umam)," *IEEE Sens. J.*, vol. 22, no. 6, pp. 5113–5121, 2022.
[15] S. Y. Cho, J. H. Lee, and C. G. Park, "A zero-velocity detection algorithm robust to various gait types for pedestrian inertial navigation," *IEEE Sens. J.*, vol. 22, no. 6, pp. 4916–4931, 2022.
[16] G. Cappellini, Y. P. Ivanenko, R. E. Poppele, and F. Lacquaniti, "Motor patterns in human walking and running," *J. Neurophysiol.*, vol. 95, no. 6, pp. 3426–3437, 2006.
[17] C. J. Chase, E. J. Aguiar, C. C. Moore, S. R. Chipkin, J. Staudenmayer, C. Tudor-Locke, and S. W. Ducharme, "Cadence (steps/min) as an indicator of the walk-to-run transition," *Hum. Mov. Sci.*, vol. 90, p. 103117, Aug. 2023.

[18] K. Kunze, P. Lukowicz, K. Partridge, and B. Begole, "Which way am i facing: Inferring horizontal device orientation from an accelerometer signal," in *2009 International Symposium on Wearable Computers*, 2009, pp. 149–150.

[19] N. Mohssen, R. Momtaz, H. Aly, and M. Youssef, "Humaine: a ubiquitous smartphone-based user heading estimation for mobile computing systems," *GeoInformatica*, vol. 21, pp. 519–548, 2017.

[20] X. Niu, T. Liu, J. Kuang, and Y. Li, "A novel position and orientation system for pedestrian indoor mobile mapping system," *IEEE Sens. J.*, vol. 21, no. 2, pp. 2104–2114, 2020.

[21] X. Niu, T. Liu, J. Kuang, Q. Zhang, and C. Guo, "Pedestrian trajectory estimation based on foot-mounted inertial navigation system for multi-story buildings in postprocessing mode," *IEEE Internet Things J.*, vol. 9, no. 9, pp. 6879–6892, 2022.

[22] T. Liu, J. Kuang, W. Ge, P. Zhang, and X. Niu, "A simple positioning system for large-scale indoor patrol inspection using foot-mounted ins, qr code control points, and smartphone," *IEEE Sens. J.*, vol. 21, no. 4, pp. 4938–4948, 2021.
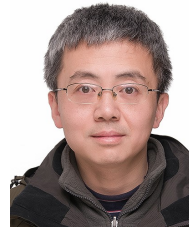
**Xiaoji Niu** got his Ph.D. and bachelor degrees from the Department of Precision Instruments at Tsinghua University in 2002 and 1997 respectively. He did post-doctoral research at the University of Calgary and worked as a senior scientist in SiRF Technology Inc. He is now a Professor of GNSS Research Center at Wuhan University in China. Dr. Niu leads a multi-sensor navigation group focuses on GNSS/INS integrations, lowcost navigation sensor fusion, and its new applications. Dr. Niu has published more than 90 academic papers and own 28 patents.

**Jian Kuang** received the B.Eng. degree and Ph.D. degree in Geodesy and Survey Engineering from Wuhan University, Wuhan, China, in 2013 and 2019, respectively. He is currently an Associate Research Fellow with the GNSS Research Center in Wuhan University, Wuhan, China. His research interests focus on vechile and pedestrian dead reckoning, and magnetic field positioning.

**Dazhou Xia** received the B.Eng. degrees in navigation engineering from Wuhan University, Wuhan, China, in 2022, where he is currently pursuing the master's degree in geodesy and surveying engineering. His research interests focus on inertial navigation, sensor fusion algorithms, pedestrian navigation and indoor positioning.

**Yan Wang** obtained his B.Eng. in Chemical Engineering and Technology from China University of Mining and Technology, Xuzhou, in 2016, followed by an M.S. in Computer Applied Technology from the same university in 2019. In 2023, he was awarded a Ph.D. from Wuhan University, Wuhan, China. He is currently conducting postdoctoral research at Wuhan University. His research concentration lies in indoor navigation, sensor fusion algorithms, and computer vision.

**Xianmei Meng** got her Ph.D degree from School of Nursing at Naval Medical University, China in 2019, and MN degree from School of Nursing, University of Calgary, Canada, in 2008. She is now an assistant professor of Nursing School at Wuhan University in China. Her major research interests are community health nursing and rehabilitation nursing. Dr. Meng has published more than 30 academic papers(one is in a TOP journal), and owned 3 patents.